Stable strontium isotopic heterogeneity in the solar system from double-spike data

B.L.A. Charlier[1,2*], I.J. Parkinson[1,3], K.W. Burton[4], M.M. Grady[1], C.J.N. Wilson[2], E.G.C. Smith[2]

1. STEM Faculty, The Open University, Milton Keynes MK7 6AA, United Kingdom
2. SGEES, Victoria University, PO Box 600, Wellington 6140, New Zealand
3. Earth Sciences, University of Bristol, Bristol BS8 1RJ, United Kingdom
4. Earth Sciences, University of Durham, Durham DH1 3LE, United Kingdom

*** Corresponding author (email: bruce.charlier@vuw.ac.nz)**

Abstract
Strontium isotopic anomalies in meteorites are important in assessing nucleosynthetic sources to, and measuring the timing of, early solar system processes. However, conventional use of a constant $^{88}Sr/^{86}Sr$ value in correcting for instrumental mass fractionation during analysis renders measurements ambiguous and removes information on mass-dependent fractionation variations. From double-spike techniques we obtain data for the four stable strontium isotopes free of this ambiguity, and report measurements from a range of meteoritic, lunar and terrestrial materials. The Earth, Moon, basaltic eucrites and feldspars from angrites (differentiated samples) follow a single mass-dependent fractionation line and have a common nucleosynthetic origin in terms of their strontium isotopes. In contrast, bulk rock CI, CV3, CM and CO chondrite samples serve to define another mass-dependent fractionation line, displaced by 94 ± 28 ppm to heavier $^{84}Sr/^{86}Sr$ and/or $^{88}Sr/^{86}Sr$ ratios than that for the differentiated samples. Our Sr-isotopic data are consistent with a primary contrast in early solar system composition between an outer zone of primitive, mostly undifferentiated, materials and an inner zone of (almost entirely) differentiated materials that accumulated to form the terrestrial planets.

Introduction
Isotopic anomalies in extraterrestrial materials hold the keys to disentangling the origins and development of the early solar system (Dauphas and Schauble, 2016; Qin and Carlson, 2016, for recent overviews). Stable strontium isotopes in particular are critical in discerning the nucleosynthetic origins of early solar system components and the timing of accretion processes. Furthermore, variations caused by high temperature mass-dependent fractionation (Young *et al.*, 2002) are also important (Patchett, 1980a,b; Moynier *et al.*, 2010; Charlier *et al.*, 2012) in providing insights into nebular and accretionary processes.

Disentangling strontium isotopic variations is problematic, however, through a first order analytical issue. Virtually all TIMS measurements of strontium isotopes employ a fixed $^{88}Sr/^{86}Sr$ ratio (8.375209) to correct for instrumental mass fractionation (IMF) during analysis (Papanastassiou and Wasserburg, 1969, 1978; Moynier *et al.*, 2010; Charlier *et al.*, 2012; Hans *et al.*, 2013). However, adoption of this fixed value precludes investigation of mass-dependent variations in the stable isotopes. In comparison, MC-ICP-MS techniques using either Zr-normalisation and/or sample-standard bracketing (Moynier *et al.*, 2010; Charlier *et al.*, 2012) can yield $^{88}Sr/^{86}Sr$ and $^{87}Sr/^{86}Sr$ ratios to examine mass-dependent fractionation effects, but cannot accurately measure $^{84}Sr/^{86}Sr$ due to ^{84}Kr interference. Most published Sr isotopic data are collectively hamstrung by one or other of these issues.

Here we present TIMS data obtained using a double-spike methodology (Rudge *et al.*, 2009) that, in contrast, recovers the abundance of the four Sr isotopes, free from any normalisation assumption (see Supplementary Information). We have measured Sr isotopes in a suite of terrestrial, lunar, and undifferentiated and differentiated meteorite samples (Table s-1). We undertook two determinations on each sample: an unspiked measurement that is IMF-corrected and a spiked measurement which, in combination with the unspiked analysis, permits us to deconvolve the absolute ratios of $^{84}Sr/^{86}Sr$, $^{88}Sr/^{86}Sr$ and $^{87}Sr/^{86}Sr$, independent of any fixed IMF correction (Neymark *et al.*, 2014). Because the uncertainties associated with the values used to derive the isotopic ratios are highly correlated, we have also considered the individual errors associated with each measurement and propagated these to derive robust error estimates (Supplementary Information).

Results and Discussion

Sr isotopic results from double spike data. We present our data in three-isotope plots ($\delta^{84/86}$Sr *versus* $\delta^{88/86}$Sr where δ represents ‰ deviation relative to NBS-987). Terrestrial samples (Fig. 1a) form a linear array that lies within error of the calculated equilibrium mass-dependent fractionation line (MDFL) produced by high temperature mass fractionation (Young *et al.*, 2002), and cluster around the bulk silicate Earth value for $\delta^{88/86}$Sr of ~+0.29 ‰ (Moynier *et al.*, 2010; Charlier *et al.*, 2012). Linear regression on our data from all terrestrial, lunar, eucrite, diogenite, and angrite samples yields a line with a slope of -0.981 ± 0.047 (Mean Square of Weighted Deviation; MSWD = 4.1) that is identical within error to the theoretical equilibrium MDFL (slope = -0.978: Young *et al.*, 2002). Our regression line (here labelled the 'terrestrial' MDFL) passes within error of the origin, indicating that these samples and their parent bodies have a nucleosynthetic Sr isotopic composition in common with Earth (and the NBS987 standard, by definition), albeit modified by high temperature mass-dependent fractionation processes (see below). Other meteorite samples show contrasting behaviour, with variations in $\delta^{88/86}$Sr and/or $\delta^{84/86}$Sr, driving the data points away from the 'terrestrial' MDFL towards heavier values (Fig. 1b). Ungrouped achondrites and carbonaceous chondrites (classes CI, CV3, CM) lie significantly to the right of the 'terrestrial' MDFL. There can be defined an apparent second MDFL from the data for the ungrouped achondrites and chondrite classes CI, CV3 and CM, together with the heavy end members of the CO and CK classes (see Table S-1 for the samples used). This second line (labelled the 'offset' MDFL) has a slope of -1.00 ± 0.21; MSWD = 7.5. This 'offset' MDFL is displaced by 94 ± 28 ppm heavier in $\delta^{84/86}$Sr or $\delta^{88/86}$Sr from the 'terrestrial' MDFL (Fig. 1b). There is a spread in the data for the ordinary chondrites and CO and CK undifferentiated samples between the two MDFLs: these data are plotted in Figure 1b, but not used to define the offset MDFL.

In general, the 'terrestrial' and 'offset' MDFLs are defined by differentiated *versus* undifferentiated materials, respectively. However, there are three exceptions to this generalisation. First, the enstatite chondrite (Abee) lies exactly on the 'terrestrial' line, despite its undifferentiated nature. Second, and in contrast, the two anomalous achondrites (NWA 011, NWA 5400) both lie within error of the 'offset' MDFL despite their differentiated nature. NWA 011 similarly plots within the 'carbonaceous chondrite' field in Cr-Ti isotopic space (see Warren, 2011). Third, the diversity seen in the ordinary chondrites and CO and CK undifferentiated samples we infer reflects the mixing within individual samples between components that have been through some kind of processing (falling on the 'terrestrial' MDFL) *versus* those not processed (falling on the 'offset' MDFL). Analysis of individual, physically separated components from these meteorites would be needed to test this inference.

Mass-dependent fractionation processes. From our work we can evaluate unambiguously the extent of mass-dependent Sr isotopic fractionation within the various reservoirs contributing to planetary materials. This can only be achieved through use of the double-spike technique. Equilibrium or kinetic fractionation effects (*e.g.,* Blanchard *et al.*, 2017; Watkins *et al.*, 2017) in the data presented here can be related to two different realms of processes. First, the fractionation that occurred during the development of the components that were assembled to produce the meteorites (regardless of their degree of differentiation). Second, magmatic processes leading to differentiation in newly forming and present-day planetary objects. The influence of 'normal' magmatic processes is seen in the spread in values along the MDFL shown by our terrestrial samples where they cover a range about half that of the entire sample suite.

Mass-independent anomalies. To allow for mass-dependent fractionation and highlight the anomalies due to either *p*-process ^{84}Sr or *r*-process-influenced ^{88}Sr, we recast our data as Δ values, *i.e.* the difference between the true value and the corresponding value along the equilibrium MDFL calculated using the true value for the other isotopic ratio (Fig. 2). If the anomalies are due solely to ^{84}Sr, the departure from the MDFL is horizontal in Figure 1, whereas if the anomaly is solely in ^{88}Sr, the offset is vertical. In practice, the numerical values for $\Delta^{84}Sr$ and $\Delta^{88}Sr$ so calculated are virtually identical because the MDFL slope is so close to 45º and the line is effectively straight across the range of values reported here. Comparison of our results with published data shows several features. The weighted mean $\Delta^{84}Sr$ of our terrestrial samples (assuming that any variation is in ^{84}Sr alone) is -0.0002 ± 0.0083 ‰ 2 s.d. (MSWD = 4.3, n = 51), and that of the terrestrial, lunar, eucrite, diogenite and angrite feldspar samples combined is -0.0018 ± 0.0060 ‰ 2 s.d. (MSWD = 4.1, n = 78), demonstrating that the NBS-987 $^{84}Sr/^{86}Sr$ composition is not at all anomalous (*cf*. Moynier *et al.*, 2012). Additionally, differences in $^{84}Sr/^{86}Sr$ proposed between Earth, Moon and enstatite chondrites versus eucrites and ordinary chondrites (Moynier et al., 2012) are not seen in our results. It is not clear how such discrepancies have arisen.

If the non-mass-dependent anomalies that we report are considered as reflecting *p*-process variations in ^{84}Sr, then several conclusions can be drawn. The elevated apparent $\Delta^{84}Sr$ values we obtain from bulk samples in CI, CV and CM chondrites (Fig. 2) cannot reflect incomplete dissolution of refractory pre-solar SiC grains, with their highly depleted ^{84}Sr (Nicolussi *et al.*, 1998; Podosek *et al.*, 2004; Paton *et al.*, 2013), as such grains are not present in concentrations that would significantly affect the bulk meteorite composition (Moynier *et al.*, 2012; Paton *et al.*, 2013). CV3 chondrites contain less SiC than CM chondrites (Huss *et al.*, 2003), yet we record a similar range in elevated apparent $\Delta^{84}Sr$ values. Two dissolutions of Murchison from separate chips of this stone also yield apparent $\Delta^{84}Sr$ values that are in close agreement. Moreover, the elevated apparent $\Delta^{84}Sr$ values in two ungrouped achondrite samples (Fig. 1b; Supplementary Information, Table S-1) reflect the bulk composition since these differentiated stones are unlikely to contain any surviving pre-solar material (Dauphas and Schauble, 2016).

^{84}Sr or ^{88}Sr anomalies?: testing for p- versus r-process anomalies in Sr. As an inescapable consequence of the number of isotopes available, there are two contrasting (but not mutually exclusive) possibilities for the origins of the non-mass-dependent behaviour in Sr: anomalies in *p*-process ^{84}Sr (*e.g.,* Moynier *et al.*, 2012) and/or in *r*-(plus *s*-)process ^{88}Sr (*e.g.,* Qin and Carlson, 2016). If the radiogenic contribution to ^{87}Sr can be accurately determined, then three-isotope plots of $(^{87}Sr/^{86}Sr)_i$ *versus* $\delta^{84/86}Sr$ and $\delta^{88/86}Sr$ should show in their deviations from a single MDFL which of the isotopes is anomalous, since the $^{87}Sr/^{86}Sr$ ratio generated by double-spike techniques will also reflect mass-dependent fractionation processes (Neymark *et al.*, 2014). The key to resolving the source of the anomalies therefore lies in determining the initial $^{87}Sr/^{86}Sr$ characteristics of the relevant materials, both without the effects of radiogenic ingrowth and accounting for mass-dependent effects. The data need to be acquired using TIMS double-spike techniques because of the requirement that the $\delta^{84/86}Sr$ ratio also needs to be accurately known in order to constrain the mass-dependent fractionation for all the Sr isotope ratios. Additionally, what is required is a suite of materials where the initial $^{87}Rb/^{86}Sr$ ratio was extremely low through formation from volatile element depleted materials (either during the initial condensation, or crystallisation from a volatile depleted melt), and any Rb present has remained undisturbed by further processing or secondary alteration. In addition, the discrimination between *p*- and *r*-process anomalies could be addressed through consideration of other isotope systems, such as Mo, Ba or Sm (*e.g.*, Brennecka *et al.*, 2013). However, the relevant data must be obtained from an aliquot of

the same dissolution as that used for the Sr isotopic analysis to avoid issues with sample heterogeneity.

The two part nature of the early solar system. Our data are consistent with previous proposals for a primary division between the materials represented by almost entirely undifferentiated, carbonaceous meteorites from the outer solar system, *versus* (almost invariably) differentiated, non-carbonaceous materials from the inner solar system (Warren, 2011; Kruijer *et al.*, 2017). This division is shown, for example, in Cr and Ti (*e.g.,* Trinquier *et al.*, 2009) and Mo and W (*e.g.,* Burkhardt *et al.*, 2012) and in our data is represented by our dual, effectively parallel MDFLs (Fig. 1a,b). Note, however, that some differentiated meteorites isotopically group with the other undifferentiated samples (Tables S-1 and S-2, Figure S-1), such as NWA011 (Warren, 2011) and NWA 5400 (Burkhardt *et al.*, 2017). In turn, our enstatite chondrite sample, although undifferentiated, falls along the terrestrial MDFL as do the lighter end members of the ordinary, CO and CM chondrites (Fig. 1a,b). Kruijer *et al.* (2017) in their proposal for a distinct contrast between inner and outer solar system domains for early-formed objects point out that differentiation sufficient to start the processes of metal separation and core formation occurred also in the outer domain. It is thus not surprising that some differentiated meteorites plot in their isotopic characteristics with the typical undifferentiated suite of materials.

The data variations that can be attributed to mass-dependent processes (*i.e.* the elongation of the data along the MDFL: Fig. 1) in turn have important implications for two aspects of early solar system history. First, our data indicate that high temperature processes have produced resolvable mass-dependent fractionation in materials that have gone to form many of the meteorite classes (both differentiated and undifferentiated) as well as within the terrestrial and lunar materials (*cf.* Simon and DePaolo, 2010). Second, contrasting interpretations (*e.g.,* Papanastassiou and Wasserburg, 1969; Halliday and Porcelli, 2001; Hans *et al.*, 2013) of the disparities in initial $^{87}Sr/^{86}Sr$ ratios in BABI, Angra dos Reis and Allende should be reconsidered. We suggest that fractionation processes (both mass-dependent and mass-independent) prior to radiogenic ^{87}Sr ingrowth must be considered as possible contributors to these disparities, rather than them simply reflecting age differences related to the timing of volatile element depletion. Also, if there is any *r*-process anomaly in ^{88}Sr, then the initial $^{87}Sr/^{86}Sr$ value is subject to the inaccuracy in any internally normalised data that employs a fixed $^{88}Sr/^{86}Sr$ ratio for IMF corrections.

Adoption of double-spike techniques is thus central to unlocking accurate, precise measurements and modelling of early solar system processes using Sr isotopes. The unique insights given by double-spike data open up new perspectives on the links between early solar system bodies, illuminating the different contributions to Sr isotopic variability from nucleosynthetic and variably coupled mass-dependent fractionation processes.

Acknowledgements
The CEPSAR isotope laboratories were supported by The Open University and NERC. We thank Sam Hammond and Manuela Fehr for help in the geochemistry laboratories, Caroline Smith (NHM, London) for samples and two anonymous reviewers for their helpful comments. Graphical abstract image credit: Victoria University of Wellington.

References
Blanchard, M., Balan, E., Schauble, E.A. (2017) Equilibrium fractionation of non-traditional stable isotopes: a molecular modeling perspective. Reviews in Mineralogy and Geochemistry 82, 27–63.

Brennecka, G.A., Borg, L.E., Wadhwa, M. (2013) Evidence for supernova injection into the solar nebula and the decoupling of r-process nucleosynthesis. Proceedings of the National Academy of Science, USA 110, 17241–17246.

Burkhardt, C., Kleine, T., Dauphas, N, Weiler, R. (2012) Origin of isotopic heterogeneity in the solar nebula by thermal processing and mixing of nebular dust. Earth and Planetary Science Letters 357–358, 298–307.

Burkhardt, C., Dauphas, N., Tang, H., Fischer-Godde, M., Qin, L., Chen, J., Rout, S., Pack, A., Heck, P., Papanastassiou, D. (2017) In search of the Earth-forming reservoir: Mineralogical, chemical, and isotopic characterizations of the ungrouped achondrite NWA 5363/NWA 5400 and selected chondrites. Meteoritics and Planetary Science 52, 807–826.

Charlier, B.L.A., Nowell, G.M., Parkinson, I.J., Kelley, S.P., Pearson, D.G., Burton, K.W. (2012) High temperature strontium stable isotope behaviour in the early solar system and planetary bodies. Earth and Planetary Science Letters 329–330, 31–40.

Dauphas, N., Schauble, E.A. (2016) Mass fractionation laws, mass-independent effects, and isotopic anomalies. Annual Review of Earth and Planetary Sciences 44, 709–783.

Halliday, A.N., Porcelli, D. (2001) In search of lost planets – the paleocosmochemistry of the inner solar system. Earth and Planetary Science Letters 192, 545–559.

Hans, U., Kleine, T., Bourdon, B. (2013) Rb–Sr chronology of volatile depletion in differentiated protoplanets: BABI, ADOR and ALL revisited. Earth and Planetary Science Letters 374, 204–214.

Huss, G.R., Meshik, A.P., Smith, J.B., Hohenberg, C.M. (2003) Presolar diamond, silicon carbide, and graphite in carbonaceous chondrites: implications for thermal processing in the solar nebula. Geochimica et Cosmochimica Acta 67, 4823–4848.

Kruijer, T.S., Burkhardt, C., Budde, G., Kleine, T. (2017) Age of Jupiter inferred from the distinct genetics and formation times of meteorites. Proceedings of the National Academy of Science, USA 114, 6712–6716.

Moynier, F., Agrainer, A., Hezel, D.C., Bouvier, A. (2010) Sr stable isotope composition of Earth, the Moon, Mars, Vesta and meteorites. Earth and Planetary Science Letters 300, 359–366.

Moynier, F., Day, J.M.D., Okui, W., Yokoyama, T., Bouvier, A., Walker, R.J., Podosek, F.A. (2012) Planetary-scale strontium isotopic heterogeneity and the age of volatile depletion of early solar system materials. Astrophysical Journal 758, 45.

Neymark, L.A., Premo, W.R., Mel'nikov, N.N., Emsbo, P. (2014) Precise determination of δ88Sr in rocks minerals and waters by double-spike TIMS: a powerful tool in the study of geological, hydrological and biological processes. Journal of Analytical Atomic Spectrometry 29, 65–75.

Nicolussi, G.K., Pellin, M.J., Lewis, R.S., Davis, A.M., Clayton, R.N., Amari, S. (1998) Strontium isotopic composition in individual circumstellar silicon carbide grains: a record of s-process nucleosynthesis. Physical Review Letters 81, 3583–3586.

Papanastassiou, D.A., Wasserburg, G.J. (1969) Initial strontium isotopic abundances and the resolution of small time differences in the formation of planetary bodies. Earth and Planetary Science Letters 5, 361–376.

Papanastassiou, D.A., Wasserburg, G.J. (1978) Strontium isotopic anomalies in the Allende meteorite. Geophysical Research Letters 5, 595–598.

Patchett, P.J. (1980a) Sr isotopic fractionation in Ca–Al inclusions from the Allende meteorite. Nature 283, 438–441.

Patchett, P.J. (1980b) Sr isotopic fractionation in Allende chondrules: a reflection of solar nebular processes. Earth and Planetary Science Letters 50, 181–188.

Paton, C., Schiller, M., Bizzarro, M. (2013) Identification of an 84Sr-depleted carrier in primitive meteorites and implications for thermal processing in the solar protoplanetary disk. Astrophysical Journal Letters 763, L40.

Podosek, F., Prombo, C., Amari, S., Lewis, R. (2004) s-process Sr isotopic compositions in presolar SiC from the Murchison meteorite. Astrophysical Journal 605, 960–965.

Qin, L., Carlson, R.W. (2016) Nucleosynthetic isotope anomalies and their cosmochemical significance. Geochemical Journal 50, 43–65.

Rudge, J.F., Reynolds, B.C., Bourdon, B. (2009) The double spike toolbox. Chemical Geology 265, 420–431.

Simon, J.I., DePaolo, D.J. (2010) Stable calcium isotopic composition of meteorites and rocky planets. Earth and Planetary Science Letters 289, 457–466.

Trinquier A., Elliott, T., Ulfbeck, D., Coath, C., Krot, A.N., Bizzarro, M. (2009) Origin of nucleosynthetic isotope heterogeneity in the solar protoplanetary disc. Science 324, 374–376.

Warren, P.H. (2011) Stable-isotopic anomalies and the accretionary assemblage of the Earth and mars: a subordinate role for carbonaceous chondrites. Earth and Planetary Science Letters 311, 93–100.

Watkins, J.M., DePaolo, D.J., Watson, E.B. (2017) Kinetic fractionation of non-traditional stable isotopes by diffusion and crystal growth reactions. Reviews in Mineralogy and Geochemistry 82, 85–125.

Young, E.D., Galy, A., Nagahara, H. (2002) Kinetic and equilibrium mass-dependent isotope fractionation laws in nature and their geochemical and cosmochemical significance. Geochimica et Cosmochimica Acta 66, 1095–1104.

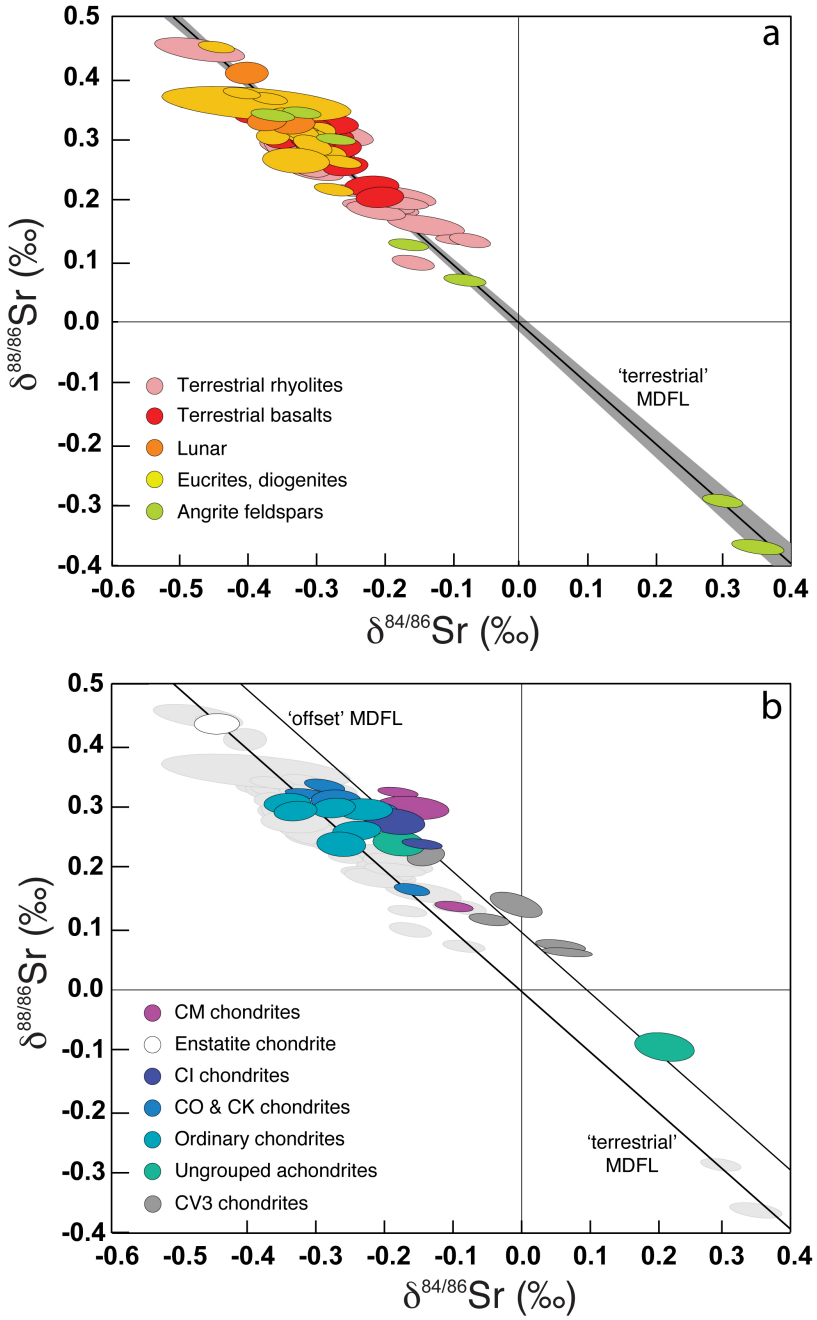

Figure 1 Three-isotope plots of all terrestrial and non-terrestrial data. **(a)** Plot of $\delta^{88/86}$Sr *vs* $\delta^{84/86}$Sr showing the data for terrestrial, lunar, eucrite, diogenite and angrite samples in this study (Supplementary Information, Table S-1). MDFL denotes the equilibrium mass-dependent fractionation line which passes through the origin (the assumed composition of NBS-987) with a slope of -0.978 (Young *et al.*, 2002). The shaded region is the 2 s.d. error envelope around the line of best fit to the data points plotted; the line itself is analytically and visually indistinguishable from the equilibrium MDFL. Data points are represented by their 2 s.d. uncertainty envelopes calculated using the methods outlined in the Supplementary Information. **(b)** Plot of $\delta^{88/86}$Sr *vs* $\delta^{84/86}$Sr showing the data measured in this study. Data points plotted in panel a are greyed out to minimise overlap. We show two lines: a 'terrestrial' MDFL which is the line of best-fit to the data points shown in panel a, and an 'offset' MDFL calculated from ungrouped achondrites and chondrite classes CI, CV3 and CM2, together with the heavy end members of the CO and ordinary chondrite classes (see Table S-2 in Supplementary Information).

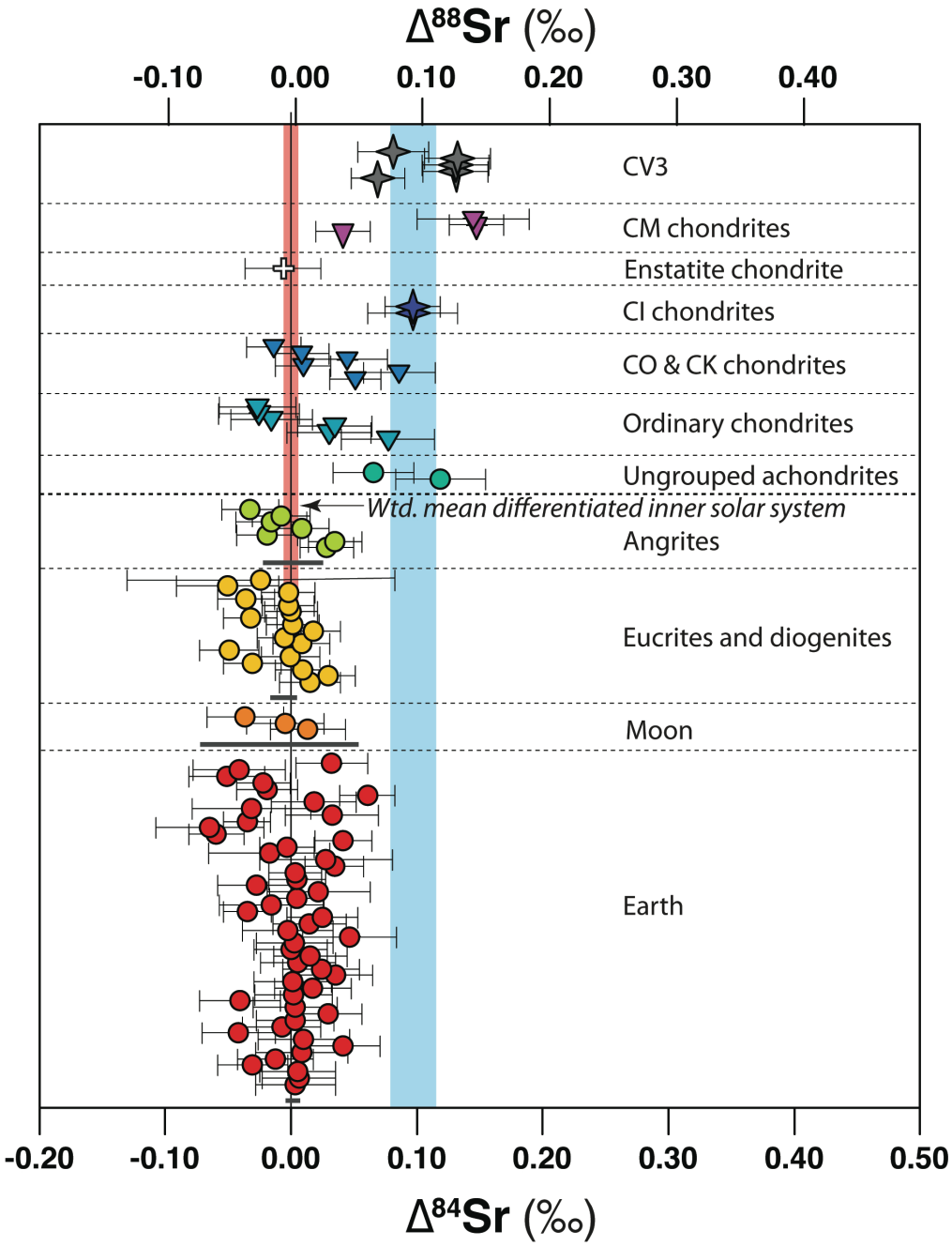

Figure 2 Plot of $\Delta^{84}Sr$ and $\Delta^{88}Sr$ for all samples (see Supplementary Information Table S-1 for data values). Uncertainties are 2 s.d., fully propagated (see Supplementary Information). Weighted mean values (±2 s.d.) for terrestrial, lunar, eucrite, diogenite and angrite samples are shown as horizontal grey bars for each of these data sets. The vertical pink bar extending through the ungrouped achondrite, ordinary chondrite and carbonaceous chondrite data is a weighted mean value (-0.0018 ± 0.0060, MSWD = 4.1) for the inner solar system derived from the terrestrial, lunar, eucrite, diogenite and angrite samples, and corresponds to the 'terrestrial' MDFL in Figure 1. The blue vertical line represents the weighted mean (±2 s.d) for the (largely undifferentiated) samples used to define the 'offset' MDFL (see text for details).

Supplementary Information

Sample Preparation, Dissolution and Chemical Separation All bulk meteorite samples, with the exception of the Smithsonian Museum Allende Reference Sample, were crushed from interior chips by hand in a new agate mortar in a class 100 clean air environment at the Open University facilities. Analytical techniques used in this study follow those established by Charlier *et al*. (2006) with an emphasis on minimising possible terrestrial contamination and optimal chemical separation techniques. Feldspar separates from the NWA angrites, and the ungrouped achondrite bulk powders, were leached in warm ~2 M HCl for 20 minutes, rinsed in 18 Ωm MilliQ water and then dried in an oven. The leaching process was carried out in order to remove the possibility of terrestrial contamination for these 'find' samples. All other bulk powders were prepared from 'falls' and were not leached. Measured sample sizes ranged from 4.64 mg for lunar sample NWA 032 to 333.1 mg for the enstatite chondrite Abee. Samples were dissolved in a 3:1 mixture of concentrated HF–HNO_3 at 130 °C on a hotplate (all reagents used were twice sub-boiling distilled in Teflon). Samples were then almost dried down before addition of aqua regia, then completely dried down before addition of 6M HCl.

Terrestrial samples were aliquots from bulk powders used for other analytical projects. All were milled in an agate Tema mill. All samples were dissolved as for the non-terrestrial samples, detailed above.

A *ca*. 10 % portion of the bulk dissolution was aliquotted for Rb and Sr concentration determination by isotope dilution (these data will be presented elsewhere). The remaining ~90 % of the bulk dissolution was then converted to nitrate form and nally equilibrated in 8 M HNO_3. This aliquot was then further divided into two equal portions, one of which was optimally spiked with our ^{84}Sr-^{87}Sr double-spike (DS), the other left unspiked. The DS and natural aliquots were then dealt with completely independently, where all further manipulations and separations were carried out in separate laminar flow cabinets and only using beakers and columns specifically designated for use with spiked and natural samples, respectively. However, the number and type of manipulations for each of the spiked and unspiked aliquots were kept identical in order to remove the possibility of differential blank issues. We also chose to spike our samples prior to column separation in order to circumvent the possible problem of column-induced fractionation. Sr was separated from both aliquots using identical protocols involving sorbing the Sr onto the resin and eluting matrix elements in 8 M HNO_3, followed by recovery of Sr in 0.05 M HNO_3. For the SiO2-rich terrestrial samples an initial Sr pre-concentration step using Biorad columns containing 2 ml AG50W-X8 resin in 2.5 M HCl was carried out.

Samples were processed in batches of 12, alongside a total procedural blank for each batch. Strontium blanks (determined by isotope dilution using a dilute ^{84}Sr single spike) never exceeded 18 pg. For all the Sr samples analysed throughout this study, no blank correction was applied since the analyte amount taken for mass spectrometry was of the order of hundreds of ng (usually *ca*. 1 μg) for both DS and natural aliquots.

Mass Spectrometry

All mass spectrometric measurements were performed using a Thermo-Finnigan Triton TIMS (thermal ionisation mass spectrometer) instrument at the Open University. The instrument is of standard configuration having 9 Faraday collectors connected to 10^{11} Ω feedback resistors. TIMS analysis for stable Sr consisted of two separate Sr isotope ratio measurements; a natural and spiked run, both made on outgassed zone-refined single Re laments. A Ta_2F_5 activator was used to maximise ionisation efficiency and natural and spiked measurements were made on separate magazines with a clean ion source extraction plate for each magazine.

Because of the relatively small abundances of three of the Sr isotopes; ^{84}Sr (0.56 %), ^{86}Sr (9.86 %), ^{87}Sr (7.00 %), it was necessary to collect a large number of ions in order to obtain high precision Sr isotope measurements. This was met by a combination of long counting times and relatively large beam intensities such that background effects are reduced on the ^{84}Sr, ^{86}Sr and ^{87}Sr. Runs were carried out using an ^{88}Sr beam intensity of 8 to 10V for 54 cycles of 10 block ratio measurements with a 16.2 second integration time.

Identical protocols were used for both the natural and spiked runs. Measurements were carried out in static mode using six amplifiers in rotation. Baselines were measured by source detection for 2 min after each step in the amplifier rotation, with a pre-baseline wait time of 30 seconds. Two cup configurations were used during the course of this study (^{88}Sr on H2, and ^{88}Sr on H1) and the amplifiers were cycled through a 'dummy' mass (set at mass ~88.5) in both cases during the measurement routine to allow the amplifier used for ^{88}Sr to fully discharge before then being connected to the Faraday cup measuring the smaller ^{84}Sr beam. Without this additional step in the rotation sequence we found that our ^{84}Sr/^{86}Sr data were systematically shifted to higher values. Correction for any ^{87}Rb interference at mass 87 was carried out using the beam intensity measured on ^{85}Rb and ^{87}Rb/^{85}Rb = 0.385707.

Natural runs were corrected for mass fractionation in the conventional way using ^{86}Sr/^{88}Sr = 0.1194. All samples were run in the course of thirteen sessions, in total spaced out over several years, with the instrument being used for other isotopic systems in between. For this reason, we report our natural and double-spike data from within the individual sessions. Analysis of 77 natural NBS 987 standards over the entire course of this study (42 months) yield a long term ^{87}Sr/^{86}Sr mean of 0.710241 (2 s.d. = 50 ppm), but the reproducibility of standard measurements within individual sessions (run within 7–10 day periods) varies between 6 and 24 ppm. Stable Sr isotope ratios were calculated using a routine similar to that detailed by Neymark *et al*. (2014) where a Newton-Raphson iteration technique implemented in MatLab was used to solve the 'true' isotope composition in ^{87}Sr denominator space for each of the ratios. Uncertainties were calculated using a 500 iteration Monte-Carlo simulation.

Our Sr double spike was prepared from enriched ^{84}Sr and ^{87}Sr spikes supplied by Oak Ridge Laboratories, resulting in an isotopic composition of ^{84}Sr = 41.94 %, ^{86}Sr = 2.28 %, ^{87}Sr = 45.53 %, ^{88}Sr = 10.26 % which was calibrated in a similar fashion to that proposed by Neymark *et al*. (2014). This double- spike composition is close to the optimal value suggested in the 'cocktail list' given by Rudge *et al*. (2009) and permits deconvolution of the 'true' isotope composition with very low error magnification over a wide range of spike-sample ratios.

Double-spike data are presented in the standard delta notation with deviations in ^{88}Sr/^{86}Sr and ^{84}Sr/^{86}Sr in per mille (‰) relative to the NBS-987 standard:

$$\delta^{88/86}Sr(‰) = \left[\frac{(^{88}Sr/^{86}Sr)_{samp}}{(^{88}Sr/^{86}Sr)_{NBS-987}} - 1\right] \times 1000$$

and

$$\delta^{84/86}Sr(‰) = \left[\frac{(^{84}Sr/^{86}Sr)_{samp}}{(^{84}Sr/^{86}Sr)_{NBS-987}} - 1\right] \times 1000$$

where $^{88}Sr/^{86}Sr_{NBS\text{-}987} = 8.375209$, and $^{84}Sr/^{86}Sr_{NBS\text{-}987} = 0.056491$.

An overall variability of thirteen separate analytical sessions of 0.132 ‰ in $\delta^{88/86}Sr$ ratios, and 0.087 ‰ in $\delta^{84/86}Sr$ ratios was observed over a period spanning 42 months. Thus, in order to account for these individual batch offsets the average of all standard measurements made in each session were normalised to $\delta^{88/86}Sr$ and $\delta^{84/86}Sr = 0$, given the values above for NBS 987, and the resulting correction factor applied to all samples and standards analysed in that batch. For each batch taken individually, the external $\delta^{84/86}Sr$ reproducibilities (2 s.d.) varied between 0.018 ‰ and 0.065 ‰, and the external $\delta^{88/86}Sr$ reproducibilities (2 s.d.) varied between 0.0096 ‰ and 0.028 ‰.

Uncertainties and Standard Data

An aspect that is often neglected is that in the three-isotope plot such as used here the uncertainties are correlated because of a common denominator isotope, in this case ^{86}Sr. For this study, we fully propagate the within-run Monte Carlo-derived uncertainties for individual samples, along with the external reproducibility of the deconvolved standards for that individual session. We also calculate a correlation coefficient and apply this to generate an error ellipse. This approach is needed because the shifts in isotopic composition we have measured are small, and we require fully propagated uncertainties to have confidence in our interpretations of the data, in particular the possible non-mass-dependent behaviour of ^{84}Sr and/or ^{88}Sr.

In conventional, internally normalised Sr isotope anal- ysis, repeated single analyses of the NBS-987 standard are used to determine the long term external reproducibility. However, with the double-spike (DS) technique this is not as straightforward. For each batch of samples, two inde- pendent measurements are required, where measurements of the natural isotopic composition are deconvolved against DS measurements made in separate analytical sessions, as described above. With each separate magazine of natural and DS samples we measure four or ve standards, respectively, with the spiked standard being a stock solution of an opti- mised mixture of our double spike and the NBS-987 standard. Rather than arbitrarily choosing an individual natural-standard combination for standard data deconvolution, we have deconvolved every possible permutation for the natural and spiked runs for each individual analysis period. Thus, for four or five natural, then DS standards run on consecutive magazines, we arrive at 16 or 25 possible ways, respectively, in which the double-spike deconvolution can be performed. We then determined a weighted mean and 2 s.d. uncertainty for this group of standards, which we then added quadratically to the individual uncertainties determined from the Monte Carlo-derived uncertainties for our unknowns in that particular batch. This method was chosen for two reasons. First, deconvolving data across disparate, non-sequential analytical sessions raises the possibility of biases due to small changes in cup efficiencies that arise over prolonged periods of time (since the TIMS instrument was used for other isotope systems). Second, it provides a robust and conservative estimate of the true external reproducibilities for our unknowns in a particular batch. Equivalence of data between disparate batches can then achieved by normalisation of the average standard value in a particular batch to the standard values (by definition $\delta^{88}Sr$ and $\delta^{84}Sr = 0$ ‰; see below) which were used in the calibration of the double spike. In this fashion, we have both confidence in the true uncertainties and accuracy of our data, as well as equivalence of data over the course of this study.

Interpretation of Standard Data

The $\delta^{88/86}$Sr *versus* $\delta^{84/86}$Sr values obtained from the multiple double-spike deconvolutions of the standards have the following properties. First, the deconvolved standard values for each batch lie close to a line (intrinsic to the measurement techniques used and the instrument behaviour) in $\delta^{88/86}$Sr *versus* $\delta^{84/86}$Sr space. Each of the lines has a near-constant slope, across all batches and natural samples within a batch, with a combined value of -44.369˚ (±0.214˚, 1 σ; 78 slope values). Second, the 'along-strike' spread of the $\delta^{88/86}$Sr *versus* $\delta^{84/86}$Sr values is constant within a batch.

These observations yield the following implications:

a. The position of the bivariate mean of $\delta^{88/86}$Sr *versus* $\delta^{84/86}$Sr values depends specifically on the choice of spikes for the deconvolution.
b. Because of the effectively constant slope of the MDFL over the range of $\delta^{88/86}$Sr *versus* $\delta^{84/86}$Sr values experienced in this work, the position of the lineation of double-spike values in the direction *at right angles* to the lineation is extremely well determined, within the measurement uncertainties of the double-spike values.
c) Similarly, because of the effectively constant slope, the distance perpendicular to the lineation will be the same irrespective of the number of double-spike values, so it has just one degree of freedom.

Calculation of Uncertainties (Confidence Ellipses) for Standard-corrected $\delta^{88/86}$Sr and $\delta^{84/86}$Sr Data

Confidence regions for the double-spike derived strontium ratios for standards

Uncertainties in double-spike method determinations of strontium ratios are typically obtained by 500 Monte Carlo simulations assuming Gaussian statistics (Neymark *et al*., 2014). The correlation coefficient for $\delta^{88/86}$Sr/$\delta^{84/86}$Sr can thus be directly calculated from the 500 simulations. These correlation coefficients are very similar across all of the batches: -0.564 ± 0.072 (2σ). The negatively signed error correlation means that confidence regions for the double-spike strontium ratios are ellipses that are slightly oblique to the MDFL.

Confidence regions for the strontium ratios of the samples

The full (Gaussian) variance matrix is calculated for each stan- dard-corrected strontium isotopic ratio, as follows.
• A full variance matrix for the sample data point is calculated from the formal 2σ uncertainties of the $\delta^{84/86}$Sr and $\delta^{88/86}$Sr data values, assuming the same (constant) correlation coefficient as the standards.
• Data for the standards, unknowns and their variances are rotated into the coordinate space parallel and perpendicular to the MDFL, so that the offset of the relevant (session by session) standard value in the perpendicular direction can be subtracted from that of the sample in the corresponding session. As the sample data and the standard data are independent, the variance matrices of the corrected data are the sum of the sample and standard data (in the rotated coordinate system).
• The corrected data and their variance matrices are then rotated back into standard, $\delta^{84/86}$Sr *versus* $\delta^{88/86}$Sr coordinates. The resulting 95 % confidence regions are ellipses which are again oblique to the MDFL (Figs 1a, b and c in the main paper).

Uncertainties in the Δ (^{84}Sr and ^{88}Sr) values

Uncertainties in the $\Delta^{84}Sr$ and $\Delta^{88}Sr$ values are calculated by Monte Carlo (MC) simulation using the full variance matrix for the data uncertainties, using the equations:

$$\Delta^{84}Sr\ (MC) = \delta^{84/86}Sr\ (MC) - 1/\tan\theta\ \delta^{88/86}Sr\ (MC)$$

$$\Delta^{88}Sr\ (MC) = \delta^{88/86}Sr\ (MC) - 1/\tan\theta\ \delta^{84/86}Sr\ (MC)$$

where θ is the slope of the terrestrial MDFL.

Supplementary Information References

Charlier, B.L.A., Ginibre, C., Morgan, D., Nowell, G.M., Pearson, D.G., Davidson, J.P., Ottley, C.J. (2006) Methods for the microsampling and high-precision analysis of strontium and rubidium isotopes at single crystal scale for petrological and geochronological applications. Chemical Geology 232, 114–133.

Neymark, L.A., Premo, W.R., Mel'nikov, N.N., Emsbo, P. (2014) Precise determination of δ88Sr in rocks minerals and waters by double-spike TIMS: a powerful tool in the study of geological, hydrological and biological processes. Journal of Analytical Atomic Spectrometry 29, 65–75.

Rudge, J.F., Reynolds, B.C., Bourdon, B. (2009) The double spike toolbox. Chemical Geology 265, 420–431.

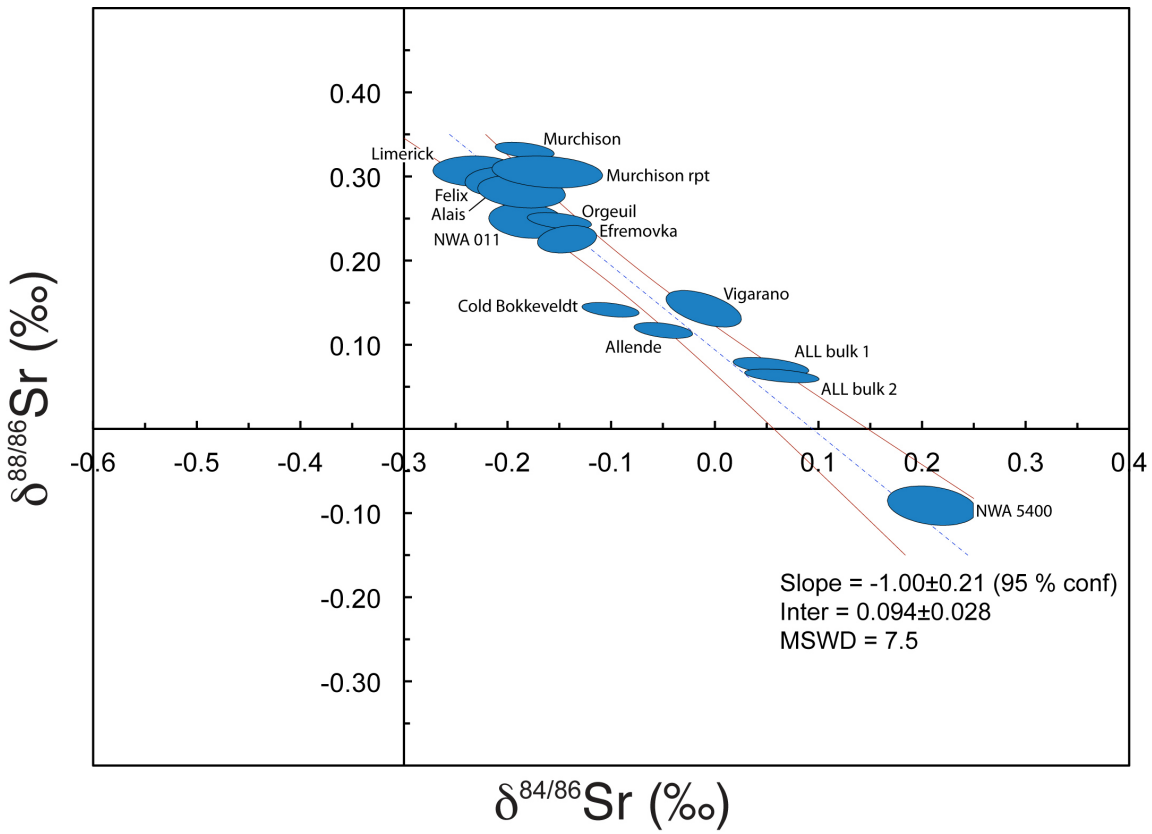

Figure S-1 Plot of δ88/86Sr vs. δ84/86Sr showing the data and best t line and error envelope for the 'offset' MDFL shown in Figure 1b.

Table S-1 Sample information and summary of Sr stable isotopic results for all samples used in this study, along with weighted means for each group of data. Details of correction for inter-batch bias, calculation of correlation coef cient and full propagation of uncertainties is given in the Supplementary Information.

Sample	Sample type	Sample weight (mg)	Batch no.	$\delta^{84/86}Sr$	2 s.d.	$\delta^{88/86}Sr$	2 s.d.	correlation coefficient	$\Delta^{84}Sr$	2 s.d.	MSWD	n
BHVO-1	Terrestrial basalt	1/4 of 35.53	9	-0.298	0.028	0.295	0.014	0.059	0.003	0.032		
BHVO-2	Terrestrial basalt	1/4 of 35.53	9	-0.305	0.024	0.305	0.013	0.163	0.006	0.029		
BHVO-3	Terrestrial basalt	1/4 of 35.53	9	-0.312	0.025	0.311	0.013	0.125	0.005	0.030		
BHVO-4	Terrestrial basalt	1/4 of 35.53	9	-0.353	0.022	0.315	0.013	0.222	-0.031	0.028		
BCR-2	Terrestrial basalt	7.98	9	-0.328	0.026	0.308	0.013	0.132	-0.012	0.030		
BIR-2	Terrestrial basalt	19.92	9	-0.297	0.033	0.298	0.013	0.063	0.008	0.037		
B	Terrestrial gabbro	16.55	9	-0.286	0.024	0.320	0.013	0.211	0.041	0.029		
C	Terrestrial gabbro	14.32	9	-0.216	0.033	0.221	0.013	0.047	0.010	0.036		
D	Terrestrial gabbro	13.68	9	-0.346	0.024	0.298	0.014	0.102	-0.042	0.029		
E	Terrestrial gabbro	15.43	9	-0.344	0.025	0.329	0.013	0.180	-0.007	0.031		
F	Terrestrial gabbro	24.03	9	-0.344	0.025	0.339	0.013	0.128	0.003	0.031		
G	Terrestrial gabbro	14.36	9	-0.275	0.023	0.298	0.013	0.252	0.029	0.027		
H	Terrestrial gabbro	15.73	9	-0.204	0.029	0.203	0.013	0.090	0.003	0.033		
EW93	Terrestrial basalt	16.41	9	-0.384	0.027	0.336	0.013	0.115	-0.041	0.032		
MD37	Terrestrial basalt	19.55	9	-0.256	0.026	0.252	0.013	0.166	0.002	0.031		
YR289	Terrestrial rhyolite	38.45	11	-0.320	0.027	0.329	0.013	-0.010	0.017	0.030		
YR291	Terrestrial rhyolite	95.28	11	-0.303	0.027	0.298	0.013	0.017	0.001	0.031		
YR292	Terrestrial rhyolite	38.08	11	-0.298	0.027	0.326	0.013	0.007	0.035	0.029		
YR294	Terrestrial rhyolite	22.75	11	-0.280	0.028	0.297	0.013	-0.005	0.024	0.030		
YR296	Terrestrial rhyolite	50.2	11	-0.302	0.026	0.300	0.013	0.037	0.005	0.030		
YR297	Terrestrial rhyolite	60.11	11	-0.306	0.024	0.314	0.013	0.051	0.015	0.029		
YR300	Terrestrial rhyolite	35.78	11	-0.297	0.027	0.290	0.013	-0.013	0.000	0.029		
YR302	Terrestrial rhyolite	50.55	11	-0.319	0.027	0.314	0.013	0.001	0.003	0.031		
YR303	Terrestrial rhyolite	41.61	11	-0.282	0.036	0.321	0.013	-0.098	0.047	0.037		
YR304	Terrestrial rhyolite	21.92	11	-0.332	0.035	0.322	0.014	-0.104	-0.003	0.036		
YR305	Terrestrial rhyolite	26.21	11	-0.306	0.026	0.314	0.014	-0.010	0.015	0.029		
YR307	Terrestrial rhyolite	90.02	11	-0.264	0.025	0.282	0.013	0.063	0.025	0.028		
YP126	Terrestrial rhyolite	13.8	1	-0.356	0.021	0.314	0.007	-0.341	-0.035	0.019		
YP127	Terrestrial rhyolite	36.46	1	-0.207	0.046	0.187	0.012	-0.500	-0.016	0.041		
YP045	Terrestrial rhyolite	35.74	1	-0.186	0.024	0.187	0.008	-0.381	0.005	0.022		
YP049	Terrestrial rhyolite	37.56	1	-0.140	0.046	0.158	0.014	-0.512	0.022	0.041		
YP053	Terrestrial rhyolite	25.56	1	-0.214	0.035	0.182	0.013	-0.493	-0.027	0.031		
YP059	Terrestrial rhyolite	21.55	1	-0.274	0.024	0.273	0.007	-0.368	0.005	0.022		
YP060	Terrestrial rhyolite	27.85	1	-0.278	0.023	0.274	0.008	-0.380	0.003	0.021		
YP061	Terrestrial rhyolite	25.77	1	-0.323	0.025	0.349	0.007	-0.353	0.035	0.023		
YP067	Terrestrial rhyolite	25.82	1	-0.290	0.060	0.311	0.019	-0.536	0.028	0.052		
YP074	Terrestrial rhyolite	15.21	1	-0.473	0.054	0.446	0.016	-0.526	-0.017	0.048		
YP079	Terrestrial rhyolite	38.41	1	-0.315	0.024	0.305	0.008	-0.398	-0.003	0.022		
YP081	Terrestrial rhyolite	45	1	-0.097	0.024	0.135	0.007	-0.331	0.041	0.023		
YP083FPG	Terrestrial rhyolite	40.23	4	-0.159	0.025	0.097	0.010	-0.440	-0.060	0.022		
YP084	Terrestrial rhyolite	16.29	1	-0.431	0.050	0.358	0.019	-0.533	-0.065	0.043		
YP131	Terrestrial rhyolite	51.57	1	-0.255	0.021	0.215	0.008	-0.367	-0.035	0.019		
YP132	Terrestrial rhyolite	29.12	1	-0.177	0.043	0.205	0.014	-0.507	0.033	0.037		
YP137	Terrestrial rhyolite	23.8	1	-0.319	0.054	0.281	0.018	-0.532	-0.031	0.047		
YP134	Terrestrial rhyolite	29.05	1	-0.182	0.037	0.196	0.009	-0.453	0.018	0.034		
YP136	Terrestrial rhyolite	54.76	1	-0.076	0.024	0.134	0.010	-0.433	0.061	0.022		
YP142	Terrestrial rhyolite	21.5	1	-0.289	0.026	0.264	0.008	-0.402	-0.019	0.024		
YP143	Terrestrial rhyolite	36.96	1	-0.281	0.023	0.253	0.007	-0.353	-0.022	0.021		
YP083SCORIA	Terrestrial basalt	6.24	1	-0.303	0.034	0.246	0.012	-0.484	-0.051	0.030		
YP079SC1	Terrestrial basalt	12.3	3	-0.329	0.043	0.281	0.036	-0.554	-0.041	0.037		
YP079SC2	Terrestrial basalt	20.38	3	-0.292	0.033	0.317	0.025	-0.543	0.032	0.029		
Wtd mean terrestrial									0.000	0.008	4.3	51
NWA 032	Lunar	4.64	12	-0.404	0.026	0.407	0.015	-0.002	0.013	0.030		
15555	Lunar	27.91	12	-0.336	0.027	0.324	0.013	0.084	-0.005	0.031		
67955	Lunar	17.92	12	-0.373	0.024	0.329	0.014	0.106	-0.036	0.031		
Wtd mean lunar									-0.009	0.063	2.8	3

Talampaya	Eucrite	40.14	2	-0.332	0.021	0.339	0.010	-0.030	0.015	0.024		
Sioux County	Eucrite	41.47	2	-0.294	0.019	0.316	0.010	-0.034	0.030	0.021		
Milliebillillie	Eucrite	28.79	2	-0.279	0.021	0.281	0.011	-0.088	0.009	0.022		
Serra de Mage	Eucrite	12.24	2	-0.368	0.022	0.329	0.010	-0.043	-0.031	0.023		
Juvinas	Eucrite	27.01	2	-0.320	0.022	0.312	0.009	-0.014	0.000	0.023		
Jonzac	Eucrite	38.43	2	-0.365	0.021	0.309	0.010	-0.043	-0.049	0.023		
Ibitera	Eucrite	24.14	2	-0.304	0.019	0.305	0.010	-0.002	0.008	0.022		
Camel Donga	Eucrite	29.63	2	-0.352	0.018	0.338	0.009	0.045	-0.006	0.021		
Agoult	Eucrite	37.59	3	-0.260	0.024	0.272	0.008	-0.435	0.018	0.021		
Bereba	Eucrite	33.34	3	-0.371	0.023	0.363	0.007	-0.413	0.001	0.021		
Emmaville	Eucrite	33.56	3	-0.412	0.023	0.371	0.007	-0.408	-0.032	0.021		
Lakangaon	Eucrite	36.99	3	-0.324	0.023	0.316	0.012	-0.495	0.000	0.021		
Moore County	Eucrite	32.4	3	-0.451	0.022	0.438	0.007	-0.408	-0.002	0.021		
Stannern	Eucrite	35.21	6	-0.273	0.024	0.231	0.008	-0.431	-0.036	0.022		
Pasamonte	Eucrite	34.19	6	-0.305	0.024	0.296	0.012	-0.494	-0.002	0.021		
Johnstown	Diogenite	153.5	10	-0.330	0.041	0.273	0.015	-0.138	-0.050	0.041		
Shalka	Diogenite	231.71	10	-0.388	0.114	0.356	0.023	-0.438	-0.024	0.107		
Wtd mean HEDs									-0.006	0.011	3.8	17
99555 fsp	Angrite	7.89	5	-0.321	0.023	0.342	0.007	-0.361	0.028	0.021		
D'Orbigny Fsp1	Angrite	4.91	5	-0.270	0.024	0.298	0.008	-0.372	0.035	0.021		
D'Orbigny Fsp2	Angrite	12.94	5	-0.364	0.027	0.337	0.008	-0.399	-0.019	0.024		
NWA 4590 fsp1	Angrite	16.92	5	0.300	0.024	-0.285	0.009	-0.413	0.008	0.022		
NWA 4590 fsp2	Angrite	18.26	5	0.352	0.032	-0.360	0.010	-0.459	-0.016	0.028		
NWA 4801 fsp1	Angrite	23.77	5	-0.080	0.025	0.071	0.008	-0.396	-0.008	0.023		
NWA 4801 fsp2	Angrite	19.34	5	-0.164	0.024	0.128	0.008	-0.388	-0.032	0.022		
Wtd mean angrite feldspars									0.002	0.024	5.1	7
Wtd mean 'differentiated'									-0.002	0.006	4.1	78
NWA5400	Ungrouped achondrite	17.86	12	0.210	0.035	-0.090	0.020	-0.254	0.119	0.036		
NWA011	Ungrouped achondrite	36.82	12	-0.182	0.031	0.242	0.017	-0.165	0.065	0.032		
Limerick	Ordinary chondrite H5	210.4	10	-0.230	0.034	0.300	0.014	-0.050	0.077	0.037		
Alfianello	Ordinary chondrite L6	205.34	10	-0.241	0.029	0.265	0.013	0.089	0.030	0.033		
Harleton	Ordinary chondrite L6	189.76	10	-0.275	0.025	0.302	0.013	0.136	0.035	0.029		
Appley Bridge	Ordinary chondrite LL6	207.35	10	-0.264	0.029	0.243	0.017	-0.108	-0.015	0.032		
Dhurmsala	Ordinary chondrite LL6	152.55	10	-0.343	0.028	0.310	0.014	0.062	-0.026	0.032		
Salles	Ordinary chondrite L5	205.58	10	-0.331	0.026	0.297	0.013	0.140	-0.027	0.031		
Wtd mean ordinary chondrites									0.009	0.042	6.1	6
Abee	Enstatite chondrite	333.1	8	-0.450	0.027	0.434	0.013	0.009	-0.006	0.030		
Kainsaz	CO3.2	180.34	6	-0.291	0.024	0.335	0.009	-0.460	0.051	0.021		
Felix	CO3.3	112.16	8	-0.209	0.024	0.289	0.014	0.035	0.086	0.029		
Ornans	CO3.4	103.89	6	-0.318	0.025	0.320	0.007	-0.429	0.010	0.022		
Moss	CO3.6	131.05	8	-0.274	0.030	0.311	0.014	-0.057	0.044	0.032		
Wtd mean CO chondrites									0.044	0.049	6.3	4
Karoonda	CK4	177.77	6	-0.161	0.023	0.166	0.008	-0.440	0.009	0.021		
Alais	CI	108.01	8	-0.185	0.035	0.276	0.016	-0.207	0.097	0.036		
Orgeuil	CI	13.78	6	-0.149	0.024	0.241	0.008	-0.430	0.097	0.022		
Wtd mean CI chondrites									0.097	0.018	-	2
Cold Bokkeveldt	CM2	119.33	6	-0.100	0.023	0.138	0.007	-0.420	0.041	0.022		
Murchison	CM2	101.1	6	-0.183	0.024	0.323	0.007	-0.424	0.148	0.022		
Murchison rpt	CM2	87.42	8	-0.161	0.044	0.299	0.015	-0.216	0.145	0.044		
Wtd mean CM2 chondrites									0.100	0.160	26	3
Allende (OU)	CV3	152.18	6	-0.049	0.023	0.116	0.008	-0.432	0.069	0.021		
ALL bulk 1 (Smithsonian)	CV3	128.37	7	0.055	0.030	0.074	0.008	-0.498	0.131	0.026		
ALL bulk 2 (Smithsonian)	CV3	115.28	7	0.067	0.029	0.062	0.006	-0.467	0.131	0.027		
Viagarano bulk	CV3	203.2	7	-0.010	0.031	0.139	0.017	-0.542	0.132	0.026		
Efremovka	CV3	100.33	10	-0.143	0.023	0.219	0.013	0.216	0.081	0.028		
Wtd mean CV3 chondrites									0.106	0.040	6.6	5
									n total	112		

Table S-2 Sr isotopic compositions for the samples used for regression of the 'offset' MDFL in Figure 1b.

		Batch no.	$\delta^{84/86}Sr$	2 s.d.	$\delta^{88/86}Sr$	2 s.d.	correlation coefficient
NWA5400	Ach ung	12	0.2105	0.0348	-0.0896	0.0196	-0.2543
NWA011	Ach ung	12	-0.1817	0.0310	0.2415	0.0172	-0.1648
Limerick	H5 chondrite	10	-0.2296	0.0337	0.2997	0.0144	-0.0505
Felix	CO3.3	8	-0.2092	0.0243	0.2885	0.0136	0.0350
Alais	CI1	8	-0.1852	0.0354	0.2756	0.0163	-0.2067
Orgeuil	CI1	6	-0.1494	0.0244	0.2405	0.0075	-0.4301
Cold Bokkeveldt	CM2	6	-0.0997	0.0227	0.1379	0.0074	-0.4198
Murchison	CM2	6	-0.1834	0.0238	0.3235	0.0074	-0.4238
Murchison rpt	CM2	8	-0.1610	0.0438	0.2990	0.0152	-0.2158
Allende	CV3	6	-0.0495	0.0232	0.1157	0.0077	-0.4316
ALL bulk 1	CV3	7	0.0554	0.0297	0.0737	0.0082	-0.4978
ALL bulk 2	CV3	7	0.0671	0.0293	0.0622	0.0065	-0.4675
Viagarano bulk	CV3	7	-0.0100	0.0308	0.1392	0.0175	-0.5422
Efremovka	CV3	10	-0.1429	0.0230	0.2192	0.0130	0.2156